

A NAVIER-STOKES/FULL POTENTIAL/FREE WAKE METHOD FOR ADVANCING MULTI-BLADED ROTORS

Mert E. Berkman Lakshmi N. Sankar
Research Assistant Regents' Professor
Georgia Institute of Technology, Atlanta, Georgia

Charles R. Berezin Michael S. Torok
Aerodynamics Engineer
Sikorsky Aircraft Corporation, Stratford, Connecticut

Abstract

A hybrid scheme for predicting three-dimensional unsteady viscous flows over isolated helicopter rotors in hover and in forward flight is introduced. The flow field is viewed in three parts; i) an inner zone surrounding each blade where wake and viscous effects are captured, ii) an outer zone away from the blades, and iii) a Lagrangean wake that lies inside the outer zone and beneath it, and induces wake effects to the outer zone. This technique is coded in a flow solver and validated through a study of hovering and advancing rotors.

Introduction

The strong wake shed from rotary wings interacts with the blades, the fuselage and in some cases with the tail rotor and causes performance and noise problems for helicopters. Particularly, in hover and low speed forward flight the wake remains in the vicinity of the vehicle and dominates rotor acoustics and vibratory loads. Therefore, this wake and its effect should be accounted for in any technique that aims to predict rotor flow field and performance.

Existing rotor CFD codes can be broadly classified into two categories according to their wake handling capabilities. First generation methods solve potential, Euler or Navier-Stokes equations coupled to an external wake model. A detailed flow solution is obtained

Copyright © 1997 by the American Helicopter Society, Inc. All rights reserved.

near the blade and the effect of far wake is typically introduced as inflow corrections from a comprehensive code. The availability of more computer power has enabled development of a second generation flow solvers where an attempt is made to capture the shed vorticity and the tip vortex entirely from first principles. These codes eliminate the need for external wake models, but require significant computer resources. However the tip vortex cannot be resolved for long distances after it is shed, due to the high levels of numerical viscosity present in these schemes, particularly on coarse grids far away from the rotor disk.

In an attempt to reduce the computer time, a hybrid Navier-Stokes/full potential method have been proposed by Berezin and Sankar [Ref. 1]. In this method, the rotor wake is captured by Eulerian approaches but is not adequately resolved away from the rotor. A vorticity embedding technique developed by Steinhoff and Ramachandran [Ref. 2] avoids the far wake diffusion by solving the full potential equations and replacing the wake by embedded vortex sheets. Moulton and Caradonna [Ref. 3] coupled this technique to a Navier-Stokes solver to form a hybrid Navier-Stokes/full potential method.

Overview of the Present Work

In this work, a hybrid method is developed for solving the flow field over multi-bladed rotors in hover or forward flight. The flow is divided into three regimes: (a) a small viscous region surrounding individual rotor blades where Navier-Stokes equations are solved, (b) a potential flow region which carries the acoustic and pressure waves generated by the rotor to far field, and (c) a Lagrangean scheme for capturing the

vorticity that leaves the viscous region and convecting it away to the far field. Figure 1 shows the Navier-Stokes and potential flow zones, and a typical tip vortex trajectory.

In the viscous region, the unsteady compressible Navier-Stokes equations are solved in a finite volume form. In the inviscid region, the isentropic potential flow equations are solved. The effect of the Lagrangean wake on the potential flow region is computed using Biot-Savart law.

The present formulation is cast as an unsteady problem, so that steady and unsteady forward flight calculations may be done with a single solver. Of course, time saving approaches such as use of local time stepping may be used in our work in hover applications to accelerate convergence.

The rest of the paper is organized as follows. The mathematical and numerical formulation are described rather briefly, since these are well developed and have been extensively published [Ref. 1,4-5]. A detailed description of how Lagrangean wake is initialized, tracked in time, and updated in strength is next given. The boundaries that separate the two zones must be carefully handled to allow pressure waves and vorticity to propagate out to the far field without false reflections at the interface. These boundary conditions are next discussed. Finally, a number of validations for a two bladed rotor tested by Caradonna and Tung [Ref. 6], for the UH-60A rotor and 3-to-1 tapered tip rotor tested by Lorber et al. [Ref. 7] in hover, and the H-34 rotor in low speed forward flight by Scheiman [Ref. 8] are presented.

Numerical Method

Computational Grid

A H-O or H-H grid is used as the computational domain. Each blade requires two blocks, one over and one under. For hover cases only one blade need to be modeled since the flow is periodic from blade to blade. The blade is assumed to be rigid, blade deformation due to loads are neglected. The cyclic pitching and flapping motion in forward flight is handled by deforming the grid at each time step so that the local blade position is matched to test conditions.

The flow field is divided into two zones. The first zone includes the inviscid “potential flow” regions away from the individual blades. The second zone

covers a small region around the individual rotor blade. In this second zone viscous effects are modeled. Figure 2 shows a close up to the grid around the UH-60A blade. The inner Navier-Stokes zone is distinguished with darker grids. For multi-bladed rotors in forward flight, there will be several such small zones as shown in Figure 3. It should be noted that at zonal interfaces there is an exact one-to-one matching of the potential flow and viscous flow zones.

Navier-Stokes Solver

The 3-D unsteady, Reynolds-averaged Navier-Stokes equations are solved in the following divergence form:

$$\begin{aligned} \frac{\partial}{\partial t} \iiint \rho dV + \iint \left[E \bar{i} + F \bar{j} + G \bar{k} \right] \cdot \bar{n} dS \\ = \iint \left[R \bar{i} + S \bar{j} + T \bar{k} \right] \cdot \bar{n} dS \end{aligned} \quad (1)$$

The equation above is valid for arbitrary, but stationary control volume. Since the control volume is changing with respect to time due to blade rotation, cyclic pitching, and flapping motion, additional terms that account for the cell face velocities are added.

The fluxes crossing the cell face are computed using a Roe solver, with flux properties evaluated at the left and right sides of a given face using a MUSCL scheme [Ref. 9]. The viscous terms are computed using algebraic averages of flow properties on either side of a cell face. The resulting non-linear algebraic system of equations for the flow properties are linearized using the information at the previous time level. The resulting linearized system is inverted using an approximate factorization scheme. Details of the solver are found in the dissertation of Bangalore [Ref. 5]. The Baldwin-Lomax model is used to model turbulence. This solver can be run on a single processor, or distributed over multiple processors or over a cluster of workstations. In the present study, the single processor version of the analysis was used.

Potential Flow Solver

The potential flow solver solves the continuity equation

$$\frac{\partial}{\partial \tau} \iiint \rho dV + \iint \rho \left[\bar{v} - \bar{v}_{\text{Grid}} \right] \cdot \bar{n} dS = 0 \quad (2)$$

The τ indicates that the time derivative is for the rate of change of mass for a control volume under consideration, regardless of its spatial location.

The flow velocity \vec{V} is made up of three components: free stream velocity, disturbance potential based velocity, and induced velocity due to embedded vortices:

$$\vec{V} = \vec{V}_\infty + \nabla\phi + \vec{q}^v \quad (3)$$

The density is assumed to be related to velocity potential through isentropic gas law, neglecting temporal variation of the induced velocity, \vec{q}^v .

A 3-D unsteady compressible potential flow solver developed by Sankar et al. [Ref. 10] is used to solve Equation set (2). It uses a three factor ADI scheme to invert the matrix system for ϕ . The potential flow solver can capture embedded weak shock waves, and can model the convection of acoustic waves in a time accurate manner. It can not, however, capture embedded vortex filaments such as embedded tip vortices. A mechanism must be therefore provided in the flow solver to model this effect.

Wake Model

A rigid or a free wake model may be used to account for the wake effects in the full potential zones. The model used in this study only considers the tip vortex, neglecting the inboard vortex sheet and trailed vorticity. In the future studies, the inner wake will be included, and an efficient procedure for the induced velocity proposed by Steinhoff and Ramachandran [Ref. 2] will be used. The helical tip vortices up to 10 revolutions are modeled by a connected series of straight line elements with azimuthal increments of 10 degrees as shown in Figure 1. The classical helical wake [Ref. 11] or Kocurek and Tangler's prescribed wake structure [Ref. 12] may be assumed to start to the solution process for hovering rotors. For advancing blades the classical wake [Ref. 11] is used to model the tip vortex structure. The strength of the tip vortex is taken to be the bound circulation at a predefined tip radial station (usually 97-99% radii) or the peak bound circulation and allowed to change from one time level to the next as the loading on the blade changes.

Given the vorticity strength and geometry, the induced velocity can be evaluated. One approach for line elements is the Biot-Savart law:

$$\vec{q}^v = \sum_{\text{elements}} \frac{\Gamma}{4\pi} \frac{d\vec{l} \times \vec{r}}{|\vec{r}|^3} \quad (4)$$

Here \vec{r} is the distance between the vortex element and the point where the induced velocity, \vec{q}^v is calculated. A Rankine vortex core model [Ref. 13] with radius of one tenth of the blade radius is used. Using Equation (4), the induced velocities at all full potential nodes are computed. The induced velocity, then is included in the potential flow analysis as shown in Equation (3). For the rigid wake model, calculation of induced velocity coefficients is done once. Based on the local blade position and the current tip vortex strength these coefficients are converted into the induced velocity field.

The free wake model causes the relaxation of the first revolution of wake elements, so that they move with the local flow velocity. The remaining wake elements are non-moving wake elements and placed appropriately based on the position of the last free wake marker. In free wake models, since the filaments move at each iteration, the induced velocity coefficients have to be updated. This calculation consumes significant CPU time. Thus it becomes prohibitively expensive to update wake information at every time step. Besides, numerous researchers had encountered "free wake instability", when they updated the wake structure continually. Therefore, in this study at every time step only the location of the filaments are tracked and the wake induced velocity coefficients are recomputed at all nodes after every 5-15 degrees of blade rotation.

Boundary Conditions

The hybrid solver requires three types of boundary conditions that must be addressed: solid surface boundary conditions at the rotor surface, far field boundary conditions, and boundary conditions for acoustic waves and vorticity that cross the Navier-Stokes/full potential interface.

Solid Surface Boundary Conditions:

The no slip conditions are enforced. For a rotor in forward flight, this simply means that the velocity of the fluid is equal to the velocity of the blade. The surface pressure and temperature gradients p/n and T/n were set to zero at the solid surface.

Far Field Boundary Conditions:

In the present approach, the far field is usually located one or more rotor diameter away from the rotor disk, and contamination of the solution due to the reflection of acoustic waves at the far field is not a major consideration. The code in its present form sets the disturbance potential ϕ to be zero at these boundaries. This assumption that all disturbances vanish at the far field boundaries, however, violates the global momentum and energy balance. For forward flight applications flow quantities at the block boundaries (lying in azimuthal planes) are transferred from block to block if all of the blades are resolved.

Boundary Conditions for Modeling Acoustic Waves and Vorticity Across the Interface:

The following coupling of Navier-Stokes and full potential zones has originally been developed by Sankar et. al. [Ref. 14] and shown to pass information through interface boundaries accurately for fixed and rotary wing solvers using C-H grids [Ref. 1,14].

The Navier-Stokes and the full potential zone are required to overlap each other at least by one node in the present approach. Consider a point P with index (i,j,k). The point immediately underneath (i,j,k-1) lies in the Navier-Stokes zone, while the point immediately above it (i,j,k+1) lies in the potential flow zone. The point (i,j,k) itself is solved for twice, once using the Navier-Stokes solver, and again using the full potential flow solver.

At the interface (i,j,k-1/2) the potential flow solver requires the density ρ and the normal velocity V_n so that the flux crossing this boundary $\rho V_n \Delta S$ can be computed. In this work these quantities were computed by averaging the Navier-Stokes values at the node (i,j,k) and the node (i,j,k-1) immediately underneath it. Thus, the Navier-Stokes code supplies a Neumann type of boundary condition to the potential flow solver for ϕ/n . The Navier-Stokes code does not transfer information about the tangential components of velocity (i.e. vorticity) directly to the potential flow solver.

The potential flow zone receives vorticity, in the form of a distributed vortical flow field. The initial portions of the tip vortex following its generation at the blade is solved for inside the Navier-Stokes zone. At the interface it is converted into a concentrated tip vortex made up of wake markers that are tracked using a Lagrangean scheme described.

When applying the Navier-Stokes solver to the node P, we need all the flow properties (ρ, u, v, w, p) at

(i,j,k+1) and at (i,j,k+2). These were obtained by computing $\nabla\phi$ using Equation (5), and then applying the energy equation to get T, and finally applying the isentropic law to get ρ and p.

$$\begin{aligned} u &= \phi_x + \bar{q}^v \cdot \bar{i} \\ v &= \phi_y + \bar{q}^v \cdot \bar{j} \\ w &= \phi_z + \bar{q}^v \cdot \bar{k} \end{aligned} \quad (5)$$

Here the derivatives ϕ_x , ϕ_y and ϕ_z were computed on curvilinear grids using classical CFD techniques.

Results and Discussion

The above algorithm has been coded and tested. Three hover applications are presented; one for a simple two-bladed rectangular rotor, and two for modern, highly twisted rotors with differing tip configurations. Finally, the H-34 helicopter forward flight data is used to perform a preliminary validation of this code for forward flight.

Caradonna-Tung Rotor in Hover

The hybrid hover solver has been tested for several non-lifting and lifting hover cases, experimentally studied by Caradonna and Tung [Ref. 6]. They considered a two bladed untwisted, rotor of rectangular planform. The blades have NACA 0012 sections and an aspect ratio of 6. Surface pressure data are available at a number of chordwise locations at several radial locations for code validation.

A H-H grid with 133 azimuthal (chordwise) nodes, 43 radial (spanwise) nodes and 62 normal nodes is used as computational domain. The domain covers half of the rotor disk, and extends one blade radius, R, above and below the rotor plane and over a half radius in spanwise direction from blade tip. Approximately 29% of the nodes fall into the Navier-Stokes zone. The Navier-Stokes zone covers half-chord upstream and half-chord downstream of the blade.

The code is first applied to a non-lifting case where no wake modeling is needed. Figure 4 compares measured surface pressures on the blade to computed values at two radial locations. The test was conducted at a tip Mach number of 0.52. Good agreement is observed, indicating successful coupling of the two zones.

The next step is the validation of the wake model. For this purpose the loads on a hovering rotor using the wake model and without any wake model are presented. Figure 5 shows the loads at two radial stations with comparisons to experimental data. As expected, the lift is overestimated drastically if wake effects are neglected. When ten revolutions of tip vortex are included, the loads are predicted accurately compared to the measurements.

Figure 6 shows the surface pressure distributions at two spanwise stations, 68% and 96% blade. The rotor has a collective pitch of 8° with a tip Mach number of 0.612. Here the free wake model is employed with the recomputation of wake geometry and associated induced velocities 11 times. The tip vortex strength at every time step is set to the current bound circulation at 97% blade. On the same plot loads obtained using rigid wake option are also given. It is seen that the free wake model improves the quality of the solution. The free wake model also captures the tip vortex position fairly well compared to experimental measurements. The tip vortex is measured to contract 10% radii and to descend 0.3R after a full blade revolution. The corresponding numerical values are 7% and 0.34R. The CPU time increase with the free wake option was roughly 10% over the rigid wake option.

UH-60A Rotor in Hover

The hover solver is next applied to a typical current generation rotor, the four bladed UH-60A rotor. The blade has an aspect ratio of 15.3 and a maximum twist of 13° . It has a rearward sweep of 20° starting from a rotor radius of 93%. The blade is made up of two airfoil sections, SC1095 as the main airfoil and SC1095R8 section in the mid-span. A close up of the H-O grid is shown in Figure 2 which covers a 90° sector in azimuthal direction. The grid has 90 points in azimuthal, 43 in spanwise and 80 normal directions. Approximately 37% of the nodes lie in the Navier-Stokes zone and typically 7 points lie inside the boundary layer.

In these calculations, the tip vortex strength was chosen initially to be the bound circulation at 99% radius. After several hundred iterations, the peak bound circulation was used as the tip vortex strength. The calculations were started with a non-contracting wake of 10 revolutions. At every 10° blade rotation wake geometry and the wake induced velocity updates were done during the marching process, as discussed previously.

Figure 7 shows the surface pressures at 4 radial stations. The rotor is at a collective pitch angle of 10° and $M_{tip} = 0.628$. The loads are in very good agreement with the experimental measurements. Figure 8 shows the spanwise normal force distribution over the blade. The numerical values are very close to experimental measurements except around 90% blade radius. The numerical value of C_T / σ 0.0084 compares well with experimental 0.0085. However, the power consumed by the rotor is overestimated by the solver. The computed torque C_Q / σ is found to be 0.00076, compared to 0.00070 from experiments.

Tapered Tip Rotor in Hover

The tapered tip rotor is very similar to the UH-60A rotor except that the tip is not swept and has a 3-to-1 taper starting at 82% radius [Ref. 7]. It has an aspect ratio of 15.3 and a dual linear twist distribution. The grid for UH-60A blade is modified to accommodate the twist and tip shape variation for this blade.

Typical chordwise pressure coefficients are compared with measurements for the tapered tip rotor in Figure 9. In these calculations the rigid wake option is used and the tip vortex position is based on Kocurek and Tangler's model [Ref. 12]. Tip Mach number is 0.628 and the collective pitch is 8.6° in this run.

H-34 Rotor in Forward Flight

The hybrid solver is finally applied to a forward flight case. The code is compared against the H-34 flight test data [Ref. 8]. The rotor has four blades with NACA 0012 sections. The blade has a linear twist of -8° and an aspect ratio of 20.48. The helicopter has a forward speed of 23 knots and advance ratio is 0.064. The blade pitching and flapping motion is defined by

$$\begin{aligned}\theta_{root} &= \theta_c + \theta_{1c} \cos \psi + \theta_{1s} \sin \psi \\ \beta &= \beta_0 + \beta_{1c} \cos \psi + \beta_{1s} \sin \psi\end{aligned}\quad (9)$$

Higher order blade harmonics are neglected. Here ψ is the azimuthal position of the blade and the pitching and flapping coefficients for the particular case are $\theta_c = 12.3^\circ$, $\theta_{1c} = 2.2^\circ$, $\theta_{1s} = -0.35^\circ$, $\beta_0 = 3.6^\circ$, $\beta_{1c} = 0.01^\circ$, $\beta_{1s} = -0.34^\circ$.

A H-O grid with 90 points in azimuthal, 44 in radial and 80 normal directions is used. The blade is

represented by 40 chordwise and 26 spanwise points. In this simulation only one blade is modeled. However, the effect of the other blades are included through the tip vortices they shed. The results presented are after two full blade revolutions. In the first revolution the tip vortex strength of the unresolved blades were taken equal to the resolved blade's strength. However, during the subsequent revolutions these strengths are updated based on the peak bound circulation of the resolved blade at that particular azimuthal location. Rigid wake option is used in this simulation and 10 revolutions of the tip vortex are modeled.

The spanwise lift distribution at 3 azimuthal stations are given in Figure 10. The lift is predicted well at $\psi = 0^\circ$. At the advancing position the lift is overestimated except near the tip. On the retreating side, the lift is predicted accurately up to 85% blade. The measured lift increases very rapidly near the tip sections which is not captured by the solver. More grid points around the tip region may improve solution accuracy. The experimental thrust coefficient, C_T is 0.005 and numerically it is found to be 0.0048.

The code has been set up for use on workstations, and has not been optimized for mainframe systems. A typical hover solution requires about 15 hours of CPU time on a HP 735 Workstation. The convergence is reached when the residuals drop three orders of magnitude or C_T value changes are very small. A typical forward flight solution, resolving only one blade, takes about 50 CPU hours for two blade revolutions. Approximately 50% CPU reduction is achieved for the test cases using the hybrid methodology (with rigid or free wake option) compared to the full blown Navier-Stokes solver without degrading the quality of the solution.

Concluding Remarks

A hybrid Navier-Stokes/full potential solver with a Lagrangean treatment of vortex wake leaving viscous zone has been developed, and preliminary validations were done. The Navier-Stokes region can be kept very small leading to lower CPU times.

Additional code validations for rotors in hover and forward flight are needed. Advancements in the methodology such as inclusion of inner wake, fifth order accurate spatial differencing scheme, and distribution of calculations over multiple processors should be done. With these enhancements, this solver

should prove to be a useful and efficient tool to the rotorcraft industry.

Acknowledgments

The first two authors were supported by a contract from the Sikorsky Aircraft Corporation and by the National Rotorcraft Technology Center (NTRC).

References

- [1] Berezin, C. R. and Sankar, L. N., "An Improved Navier-Stokes/Full Potential Coupled Analysis for Rotors," *Mathematical Computational Modeling*, Vol. 19, No. 3/4, 1994, pp. 125-133.
- [2] Steinhoff, J. and Ramachandran, K., "Free-Wake Analysis of Compressible Rotor Flows," *AIAA Journal*, Vol. 28, No. 2, 1989, pp. 426-431.
- [3] Moulton, M., Hafez, M., Caradonna, F., "Zonal Procedure for Predicting the Hovering Performance of a Helicopter," *ASME Journal*, Vol. 184, 1984.
- [4] Berkman, M. E., Sankar, L. N., Berezin, C. R., Torok, M. S., "A Navier-Stokes/Full Potential/Free Wake Method for Rotor Flows," *AIAA Paper 97-0401*, Jan. 1997.
- [5] Bangalore, A. and Sankar, L. N., "Forward Flight Analysis of Slatted Rotors Using Navier-Stokes Methods," *AIAA Paper 96-0675*, Jan. 1996.
- [6] Caradonna, F. X. and Tung, C., "Experimental and Analytical Studies of a Model Helicopter Rotor in Hover," *NASA TM-81232*, 1981.
- [7] Lorber, P. F., Stauter, R. C., and Landgrebe, A. J., "A Comprehensive Hover Test of the Airloads and Airflow of an Extensively Instrumented Model Helicopter Rotor," *Proceedings of 45th Annual Forum of the American Helicopter Society*, MA, May, 1989.
- [8] Scheiman, J., "A Tabulation of Helicopter Rotor-Blade Differential Pressures, Stresses and Motions as Measured in Flight," *NASA TM X-952*, Mar. 1964.
- [9] Van Leer, B., "Towards the Ultimate Conservative Difference Scheme, a Second Order Sequel to Godunov's Method," *Journal of Computational Physics*, Vol. 32, 1979.
- [10] Sankar, L., Malone, J., Tassa, Y., "An Implicit, Conservative Algorithm for Steady and Unsteady Transonic Potential Flows," *Proceedings of the AIAA 5th Computational Fluid Dynamics Conference*, 1981.
- [11] Johnson, W., *Helicopter Theory*, Princeton University Press, New Jersey, 1980.
- [12] Kocurek, J. D. and Tangler, J. L., "A Prescribed Wake Lifting Surface Hover Performance Analysis," *Proceedings of 32nd Annual Forum of the American Helicopter Society*, May, 1976.

[13] U.S. Department of the Army - Aeroflightdynamics Directorate, "2GCHAS Theory Manual," Vol. II, Chp. 5, Ames Research Center, Moffet Field, CA, July, 1992.

[14] Sankar, L. N., Bharadvaj, B. K., and Tsung, F.-L., "Three-Dimensional Navier-Stokes/Full Potential Coupled Analysis for Transonic Viscous Flow", AIAA Journal, Vol. 31 No. 10, 1993.

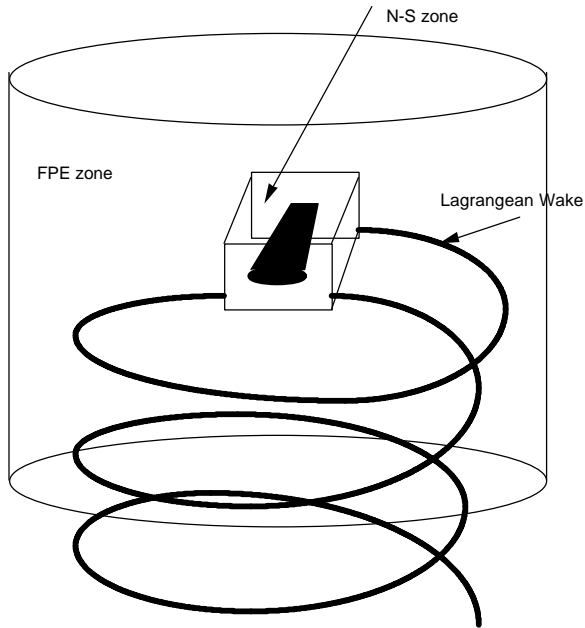


Figure 1: The three regimes of the flow field

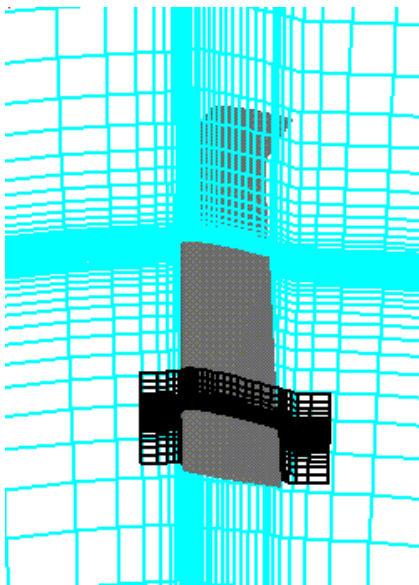


Figure 2: Grid for four bladed UH-60A rotor

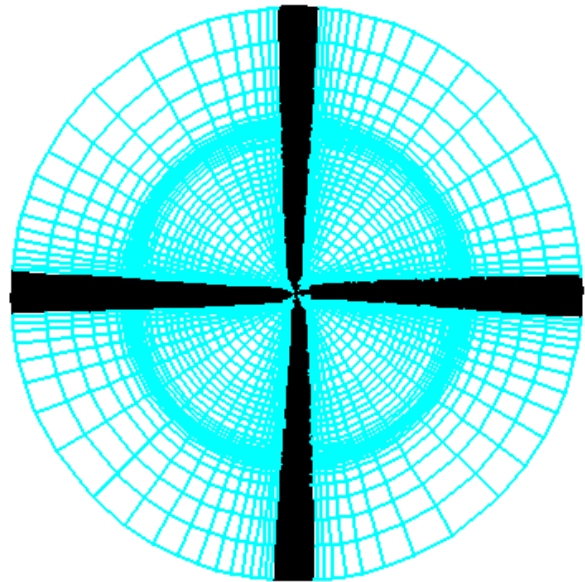


Figure 3: Grid for a four bladed rotor in forward flight, rotor plane

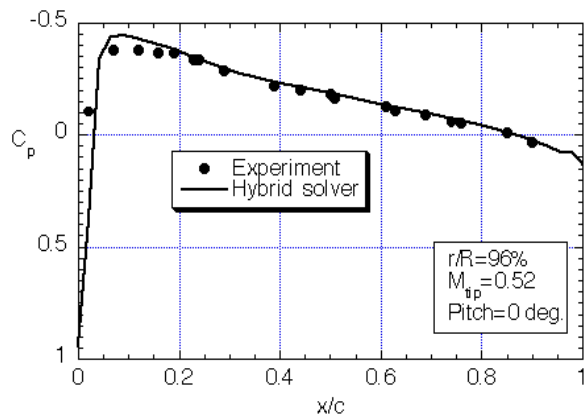
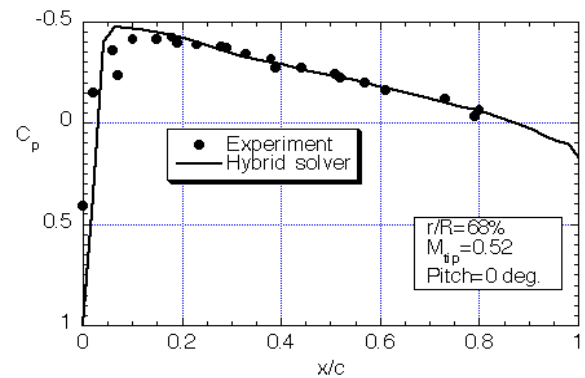


Figure 4: Surface pressures at $r/R=0.68$ and 0.96 , Caradonna-Tung rotor, $M_{tip} = 0.52$, $\theta_c = 0^\circ$

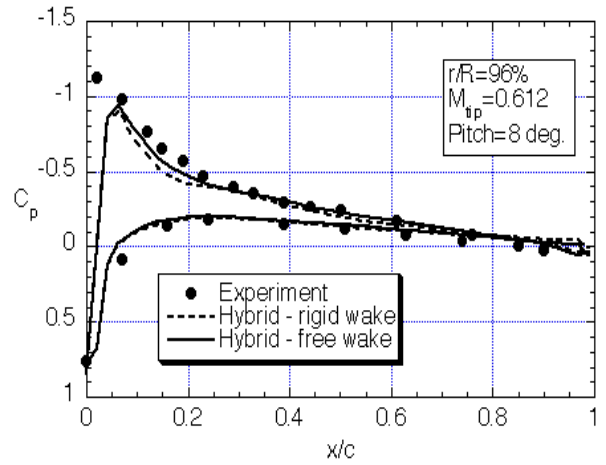
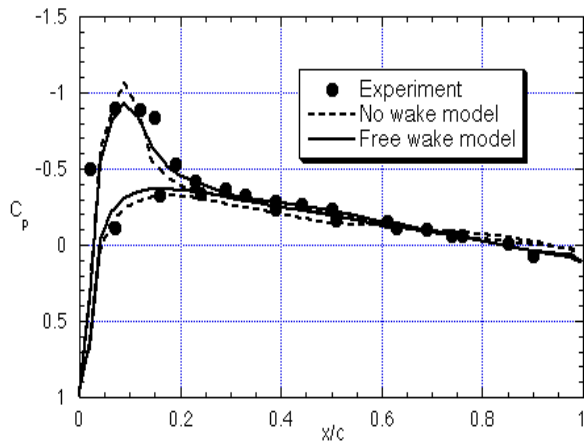
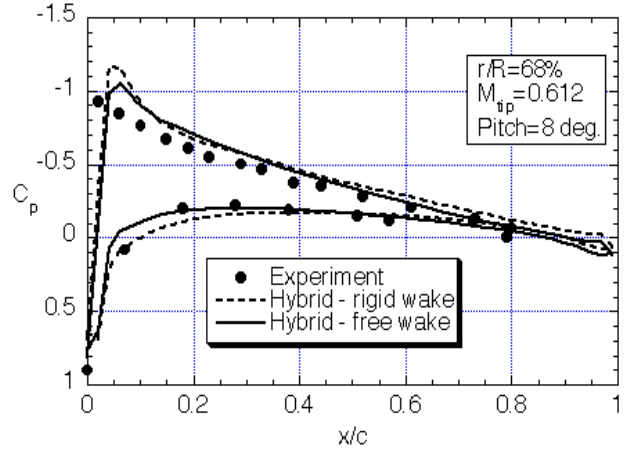
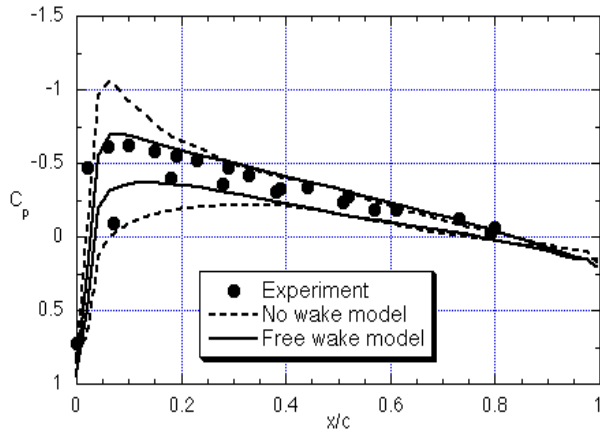


Figure 5: Surface pressures at $r/R=0.68$ and 0.96 , Caradonna-Tung rotor, $M_{tip} = 0.794$, $\theta_c = 5^\circ$

Figure 6: Surface pressure coefficients at $r/R=0.68$ and $r/R=0.96$, Caradonna-Tung rotor, $M_{tip} = 0.612$, $\theta_c = 8^\circ$

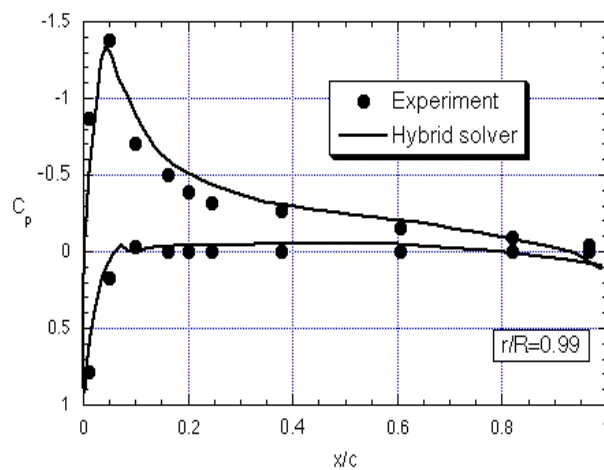
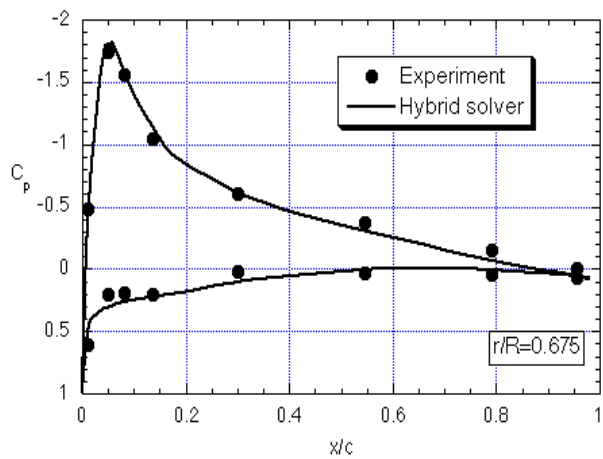
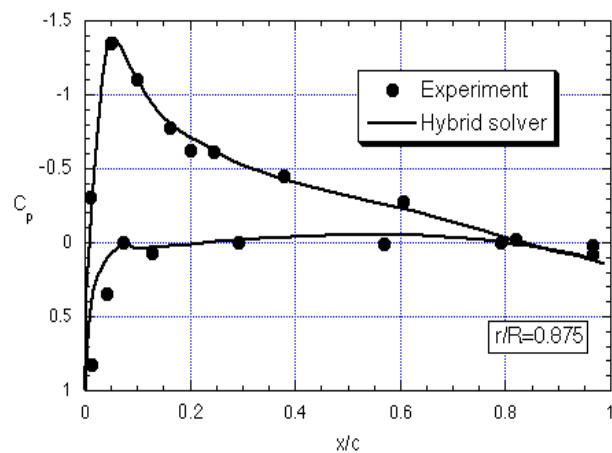
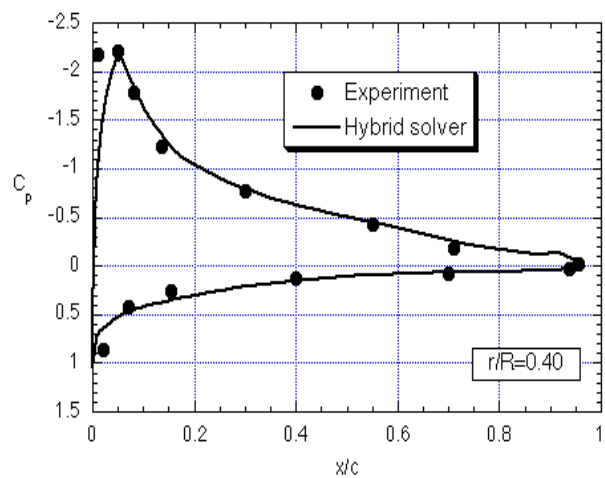


Figure 7: Surface pressure coefficients at different radial stations, UH-60A rotor, $M_{tip} = 0.628$, $\theta_c = 10^\circ$

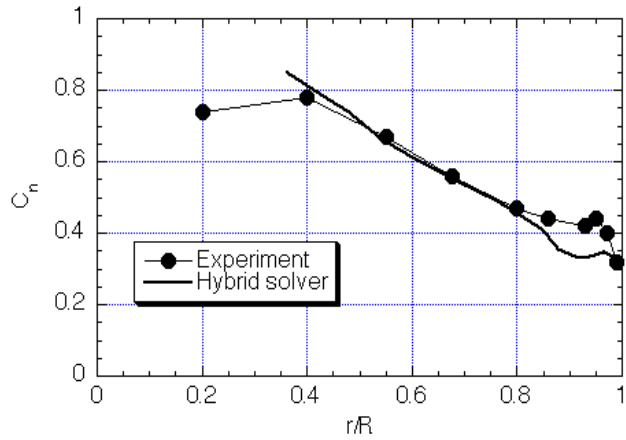


Figure 8: Sectional normal force coefficient variation along the UH-60A blade, $M_{tip} = 0.628$, $\theta_c = 10^\circ$

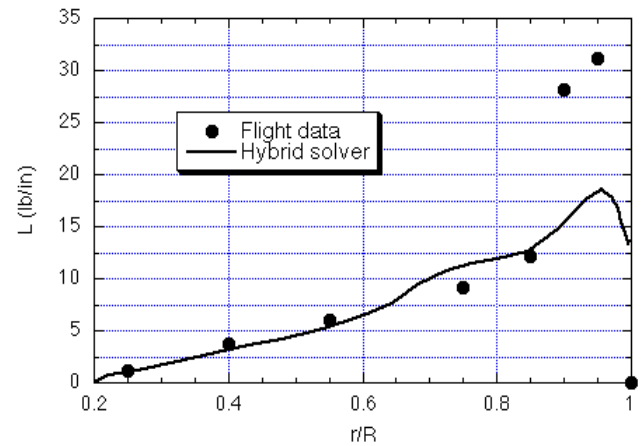
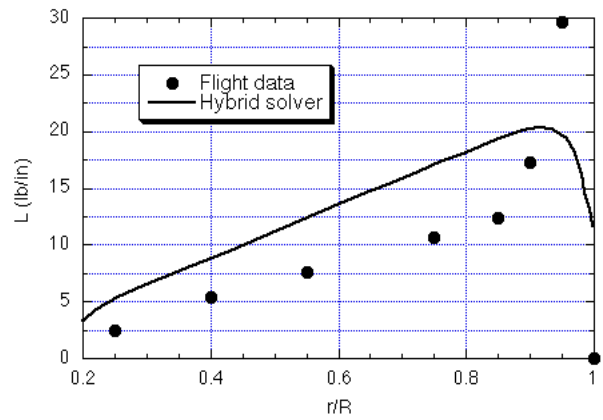
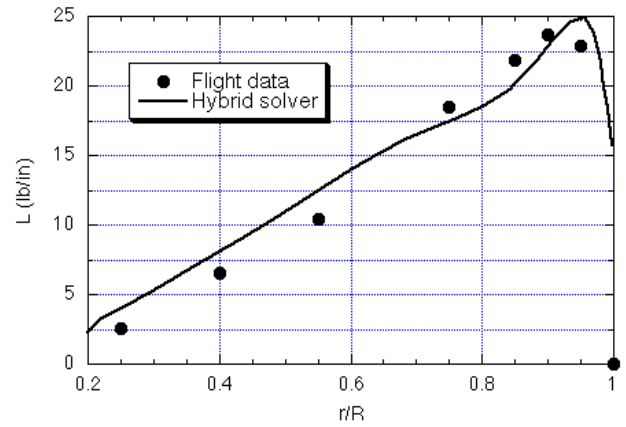


Figure 10: Lift variation along the blade at backward, advancing and retreating blade positions, $\psi = 0^\circ, 90^\circ, 270^\circ$; H-34 rotor, $\mu = 0.064$

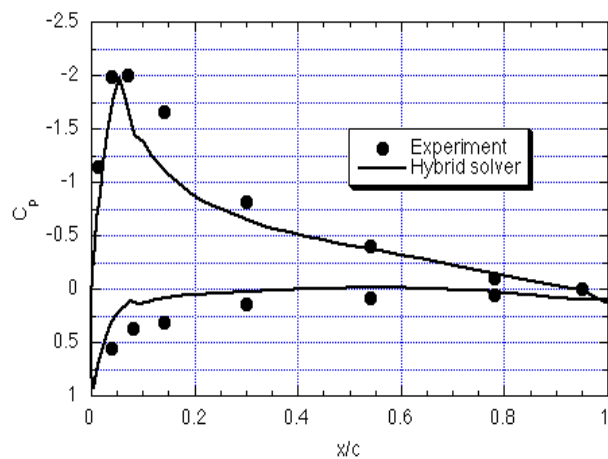
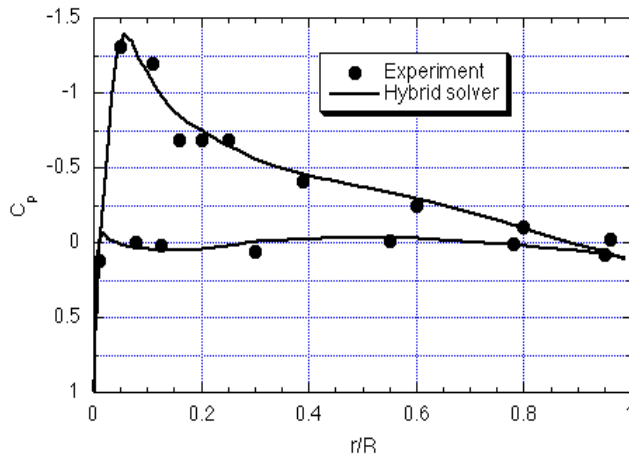


Figure 9: Surface pressure coefficients at $r/R=0.775$ and 0.945 ; Tapered tip rotor, $M_{tip} = 0.628$, $\theta_c = 8.6^\circ$